Size-dependent resistivity in a micro-processed YBa$_2$Cu$_3$O$_{7-\delta}$ superconducting whisker

Marco De La Pierre[1], Stefano Cagliero[1], Angelo Agostino[2], Gian Carlo Gazzadi[3] and Marco Truccato[1]

[1] Dipartimento di Fisica Sperimentale, NIS-Centre of Excellence and CNISM UdR Torino Università - Via P. Giuria 1, I-10125, Torino, Italy
[2] Dipartimento di Chimica Generale ed Organica Applicata, NIS-Centre of Excellence and CNISM UdR Torino Università - Corso M. D'Azeglio 48, I-10125, Torino, Italy
[3] CNR-INFM-National Research Center on nanoStructures and bioSystems at Surfaces-S3 - Via G. Campi 213/A, I-41100, Modena, Italy

E-mail: `truccato@to.infn.it`

Abstract. We report the results of a detailed geometrical and electrical study which has been performed on a YBa$_2$Cu$_3$O$_{7-\delta}$ superconducting whisker. This sample has undergone three subsequent steps of micro-machining by means of a FIB instrument, in order to progressively decrease its cross-section area from $\sim 77\ \mu$m^2 to $\sim 4\ \mu$m^2, over a length of about 150 μm. A simple analytical model based on the exact shape both of the electrical contacts and of the micro-machined material has been proposed for the voltage drop; besides, an accurate geometrical characterization of all of the sample details has been performed by means of SEM microscopy. This enabled us to extract accurate electrical resistivity curves from the resistance versus temperature characteristics for each of the fabrication steps of the whisker, showing an increase of the sheet resistivity with decreasing the cross-section area. Among the possible physical reasons for such behaviour, the inelastic electron scattering at the sample surfaces has been ruled out because of the very short mean free path of carriers in YBCO. On the other hand, oxygen out-diffusion and Ga ion implantation due to the FIB processing are most likely responsible for the observed resistivity trend.

1. Introduction

Since the discovery of high-temperature superconductors (HTSC) in 1986 [1], a lot of research has been carried out in order to clarify the microscopic mechanisms underlying their unconventional properties, but, presently, a comprehensive and fully self-consistent picture of them has not been achieved yet. Among the open questions, the role of the thermodynamic fluctuations from the equilibrium state and their influence on the unusual normal-state properties above T_c, the so-called pseudogap state, is presently unclear [2]. A possible way to study these effects is represented by the measurement of

the paraconductivity, which is the excess conductivity induced above T_c by metastable Cooper pairs. The whisker-like crystals are nearly ideal systems for this kind of studies: their very large aspect ratio ($\approx$ 100) between their length and thickness has been reported to result in an enhancement of the fluctuation phenomena; besides, this kind of samples shows a considerably lower density of defects in comparison with bulk ones [3, 4].

In the past, conductivity and paraconductivity properties of HTSC compounds have been proved to depend on the cross-section area of the crystals [5, 6] in a counter-intuitive way, so that both of them increased with decreasing the cross-section area. However, these experiments have been carried out by comparing different crystals, and no microscopic interpretation has been given for such phenomenon. Therefore, the use of Focused Ion Beam (FIB) machining to reduce the cross-section area on the *same* HTSC crystal in controlled steps is an ideal test to confirm this phenomenon and to understand what are the microscopic mechanisms possibly responsible for it. Indeed, since FIB processing is based on material sputtering by a nano-sized ion beam, it offers a quick and versatile approach to micro- and nano-structuring of virtually any material. In this technique the ion erosion is applied in the desired pattern directly on the sample as it is [7], which is a major advantage compared to the multiple and complex steps of resist-based lithographies. This feature turns out to be particularly useful for those critical materials, like HTSC, whose properties can be significantly altered by undergoing temperature or chemical etching cycles.

Actually, in the past many studies have been devoted to the development of lithographic techniques for HTSC able to achieve even submicrometric resolution, which is a key element for the fabrication of a new generation of micro-devices, like for instance THz receivers or Superconducting QUantum Interference Devices (SQUIDs). Among them, the UV sensitive sol-gel technique [8] and the electron beam lithography, both in the standard [9] and in the C_{60}-deposition assisted version [10], appear to be very interesting. Nevertheless, they have proved to suffer from material degradation processes when approaching the sub-micrometer resolution, so that the technological problem of obtaining large critical current densities on such a small scale is still open. As a complementary approach, the use of the FIB etching technique has been proposed to fabricate the desired sample shape and size, especially starting from whisker crystals. Specialized machining techniques have been developed for this purpose [11, 12], but it is also expected that FIB energetic ions introduce side-effects such as structural damage and ion implantation that have to be carefully considered and tested [13] before coming to the application stage. Therefore, the nature and the extent of the crystal modifications induced in the material characteristics by the FIB etching is an important issue which is worth further investigating.

This has been done in the present work by using a $YBa_2Cu_3O_{7-\delta}$ (YBCO) whisker sample and performing three subsequent steps of mechanical processing by means of FIB technology, in order to progressively decrease its cross-section area. An electrical characterization has been performed for each of the four resulting cross-section areas

and a detailed morphological and geometrical analysis has been carried out in each case. Some simple geometrical models are introduced to understand the effects induced by the FIB erosion on the whisker sample. Such models are then used to convert the experimental resistance curves into the resistivity ones, so that an investigation of the intrinsic electrical properties of the same YBCO crystal as a function of its cross-section area is obtained.

2. Experimental details

YBCO whisker samples were synthesized by our group according to the procedure proposed by Nagao *et al* [14]. Details of the synthesis procedure have been previously reported by Rahman Khan *et al* [15]. Among the set of synthesized whiskers, a very regular and linear crystal was selected, which did not show macroscopic surface defects (see Figure 1). The crystal was positioned on an Al_2O_3 substrate, with one of the largest surfaces adherent to the substrate. Silver plus gold electrodes were deposited on the top surface, according to a standard four-probe measurement setup [16].

Three subsequent steps of mechanical processing were performed by means of a FEI Strata^{TM} DB 235 Dual Beam workstation, in order to narrow the crystal and therefore to progressively reduce its cross-section area in the electrically probed region between the two voltage contacts, as shown in Figure 2. The Dual Beam instrument combines a high-resolution SEM and a Ga-ion FIB in a single platform. The system is designed with the SEM column along the vertical axis and the FIB one tilted by 52°, so that the two beams are coincident on the sample position. This allows easy SEM inspection during the FIB machining. As a preliminary step we evaluated the sputtering rate of YBCO under the 30 keV Ga ion irradiation, in order to choose a suitable beam current for sample processing. A box-pattern was milled in a region outside the test area and the erosion depth was measured by tilted SEM imaging of the pattern edge. We measured an erosion rate of 0.33 μm^3/nC and therefore chose a beam current of 5 nA, which was high enough to ensure a reasonable time (minutes) for the machining steps.

FIB machining was performed with the ion beam perpendicular to the sample, i.e. with the sample tilted by $\alpha = 52°$. To reduce the cross-section area, the first step was to mill two rectangular patterns, symmetric with respect to the longest whisker axis, as shown in Figure 2(b). The subsequent steps, shown in Figures 2(c) and 2(d), consisted of etching the bottom side of the whisker by scanning the FIB along a horizontal line that spanned the whole whisker length, and by progressively moving it into the whisker until the desired width was reached. This etching procedure is known as sidewall polishing.

For each fabrication step, in-situ micrographs were collected by the high-resolution SEM coupled to the FIB column; some more micrographs were collected by means of a LEICA Stereo Scan 410-Leo SRV-32 SEM to cross-check all of the measurements of the relevant sample sizes. Both microscopes featured a calibrated grid allowing an accurate measurement of the sample sizes.

After each patterning step, a characterization of the sample in-plane resistance was

performed as a function of temperature in the range $77 \div 295$ K in a liquid nitrogen cryostat by means of a standard four-probe technique. Data were collected while heating the sample in steps of $0.2 \div 0.5$ K every 130 s; the average of the readings collected in ten subsequent current reversals at the rate of 1 Hz was performed in order to cancel the thermal emfs. Feeding currents values were in the range $1 \div 10 \, \mu$A, so that corresponding current density values were kept in the range $13 \div 50$ A/cm^2.

3. Results and discussion

In order to obtain the electrical resistivity, an accurate geometrical characterization is necessary both of the longitudinal and of the cross-section sizes of the sample for all of the fabrication steps that have been performed during this work.

3.1. Determination of the cross-section area

Much care is required in measuring the cross-section area of the electrically probed region of the sample, which has been largely reduced by means of ion beam machining; in fact its very small size can lead to large relative errors. Figure 3 shows the sample after one of the FIB processes at two different tilting angles; similar pictures have been taken after each of the fabrication steps. A careful analysis based on the position of surface defects reveals that a picture with a simple rectangular cross-section shape is not adequate in the case of our sample. More reliable results can be achieved by assuming a trapezoidal shape, as shown in Figure 4.

To estimate the cross-section area according to the proposed picture, we have assumed that all of the fabrication steps have the same thickness value and that the possible tilting of the crystal with respect to the substrate is so small ($\sim 1°$) that can be included in the uncertainties of the tilting angles.

The thickness of the whisker can be calculated by $t = d \sin \theta$. Although d and θ cannot be measured within a single SEM observation, they can be evaluated by solving the trigonometric system (1):

$$\begin{cases} x_1 = d \cos (\theta - \alpha_1) \\ x_2 = d \cos (\theta - \alpha_2) \end{cases} \tag{1}$$

where the projections x_i can be measured from a couple of SEM micrographs taken at different tilting angles α_i (see Figure 3). In order to get a reliable estimate for the thickness, this procedure has been applied to seven different pairs of projections; the resulting average value is $t = (3.55 \pm 0.20) \, \mu m$.

Some important remarks can be made on this estimation. For instance, it should be noticed that each pair of projections comes from a top view (0° tilting) and a tilted view of the sample; the tilted views have been taken at different angles: 30°, 45° and 52°. The fact that the corresponding calculated quantities are in good agreement among them confirms that the picture we have given for the sample shape is good. Furthermore, by solving the system (1), an estimation for the inclination angle of the sidewall is

also obtained: $\theta = (83.6 \pm 0.9)°$. This measurement is in good agreement with the ones found in literature for similar ion beam currents and milling conditions [17, 18]. Actually, this inclination is a known effect in FIB machining, mainly due to the gaussian-like profile of the ion beam current which is transferred to the edges and sidewalls of the patterned structures. The beam profile, and especially its external tails, results in rounding the edges and in sloping the sidewalls, determining the effective sharpness of the cut [17]. These features are more pronounced the larger the beam current is, as a consequence of the beam broadening and of the increasing extension of the tails. In principle, another possible factor involved in the sidewall inclination could be the re-deposition of sputtered material. This effect usually occurs in closed patterns, where the material removed beyond a critical depth cannot escape outside the pit and is re-deposited on the sidewalls. However, in our case, this phenomenon should not be significant since in the polishing procedure the removed material is ejected behind the advancing scan line.

Therefore, the trapezoidal cross-section area after each of the three machining steps can be estimated; values for the major base b_M and the minor base b_m have been measured from the sample top views and are reported in Table 1. The calculated values for the cross-sections S' are reported in Table 2.

Concerning the sample in the as-grown condition, its rectangular cross-section area is calculated by assuming for the thickness the same value as the other processing steps and for the width a measured value of $w = (22.35 \pm 0.21)$ μm. Since the crystal turned out to have carved edges, an estimation has been made of the corresponding cross-section area reduction, by using a trigonometric procedure similar to the one used for thickness calculation; as a result, each carved edge reduces the cross-section of about 0.5 μm^2. Then, the best estimation of the cross-section area for the sample in the as-grown condition is $S = (w \cdot t - 2)$ μm$^2 = (77 \pm 4)$ μm^2.

3.2. Accounting for the contacts geometry

In our experimental setup the electrical contacts and the whisker have comparable sizes; thus, the point contact approximation must be avoided, and it becomes necessary to take into account the contact shape and sizes in order to obtain the correct relationship between the voltage drop, measured between the two voltage contacts, and the resistivity.

The voltage measurement between the two voltage contacts A and B is equal to $\Delta V = V_A - V_B$, where V_A and V_B are the the voltages corresponding to contact A and B, respectively, and can be calculated by means of the general equation:

$$V = \frac{\int \int_\Sigma V(\mathbf{r}) \, \mathrm{d}\Sigma}{\Sigma} \tag{2}$$

where $V(\mathbf{r})$ is the local value of the electrical potential and Σ is the area of either A or B contact. Considering a simple case where the current flows along the length of the sample (x-axis) only, the assumption can be made that the current density and the

electric field have non-zero components only along this axis; therefore, $V(\mathbf{r})$ depends only on x. Actually, it is well-known that HTSC compounds have a strong anisotropy between in-plane (ρ_{ab}) and out-of-plane (ρ_c) resistivities and it has been clearly shown that such anisotropy induces some voltage drop along the sample thickness direction, when the current is injected from contacts placed on the top surface, like in the present case [19]. Nevertheless, it has also been reported that, even in the case of large anisotropy ($\rho_c/\rho_{ab} \sim 10^4 \div 10^5$) like the one of the BSCCO compound, the whisker geometry causes the thickness component of the potential to induce only very small relative corrections ($< 4 \cdot 10^{-7}$) to this sample picture, which can be safely neglected [20]. On the other hand, concerning the crystal geometry after the FIB processing steps, the present model is not able to consider the effect of the current redistribution that certainly occurs at both ends of the central stricture and that induces some non-vanishing component of the potential also in the in-plane direction perpendicular to the x-axis. Within the limits of the present approximation, the following expression can be found for $V(x)$ from the microscopic Ohm's law:

$$V(x) = \int_0^x \mathrm{d}V = -\int_0^x \rho(x') \frac{I}{S(x')} \, \mathrm{d}x' \tag{3}$$

where I is the injected current, S is the sample cross-section and ρ is the component of the resistivity tensor along the x-axis. It is worth noting that, if S changes in steps along the sample length (i.e. $S = S(x)$), the integral in the right hand side of (3) must be divided in parts, each one having a constant S and that, in this case, in principle, different ρ values should correspond to different S values. In order to get an expression for ΔV, we have to write $V(x)$ explicitly for our sample, and then to solve equation (2) for each contact.

In the case of the sample in the as-grown condition, the cross-section S is constant along all the sample and the voltage contact surfaces have a simple rectangular shape (see Figure 1); therefore, we get the trivial expression for the voltage drop $\Delta V = \rho_0 IL/S$, where L is the distance from the mid-points of the two rectangular contacts, whose measured value is $L = (166.2 \pm 1.7) \, \mu$m, and ρ_0 is the constant resistivity value corresponding to the as-grown cross-section area S.

The analysis of the sample after the FIB processing steps requires some care; Figure 5 shows a schematic representation of the corresponding contact geometry. Some important features can be stressed for this geometry: i) along the sample length, three adjacent regions with two different cross-section areas (S and S') can be identified, implying that the expressions for $V(x)$ are different for these three regions; ii) in principle, different resistivities must be assumed for regions with different cross-section areas, ρ_0 representing the resistivity of the original crystal and ρ_i the resistivity corresponding to the i-th machining step (this issue will be discussed in Section 3.3); iii) the contact surface areas Σ have a non-trivial shape, being made up by two adjacent rectangles.

By solving equation (3) and imposing the continuity of the electrical potential between different regions, the following expressions for $V(x)$ are obtained for the i-th machining

step:

$$V_1(x) = -\rho_0 \frac{I}{S} x \qquad 0 \le x \le c_1 \tag{4}$$

$$V_2(x) = -\rho_0 \frac{I}{S} c_1 - \rho_i \frac{I}{S'} (x - c_1) \qquad c_1 \le x \le c_1 + c_2 + c_{mid} + c_3 \tag{5}$$

$$V_3(x) = -\rho_i \frac{I}{S'} (c_2 + c_{mid} + c_3)$$
$$-\rho_0 \frac{I}{S} [x - (c_2 + c_{mid} + c_3)] \qquad c_1 + c_2 + c_{mid} + c_3 \le x \le c_4 , \tag{6}$$

where c_1, c_2, c_3, c_4 and c_{mid} are defined according to Figure 5. The mean electrical potential for each voltage contact can then be calculated by integrating $V(x)$ over the corresponding contact area, according to equation (2). We finally obtain the following expression for the voltage drop:

$$\Delta V = \frac{I}{S'} \left(\rho_0 L_{\text{eff}}^{\alpha} + \rho_i L_{\text{eff}}^{\beta} \right) \tag{7}$$

where:

$$L_{\text{eff}}^{\alpha} = \frac{S'}{S} c_1 + w \frac{S'}{S} \frac{c_4^2}{2} / (w' c_3 + w c_4)$$
$$- (w \frac{S'}{S} \frac{c_1^2}{2} + w' \frac{S'}{S} c_1 c_2) / (w c_1 + w' c_2) , \tag{8}$$

$$L_{\text{eff}}^{\beta} = (c_2 + c_{mid}) + (w' \frac{c_3^2}{2} + w c_3 c_4) / (w' c_3 + w c_4)$$
$$- w' \frac{c_2^2}{2} / (w c_1 + w' c_2) , \tag{9}$$

and w and w' represent the width of the metal contact in the wide and narrow region, respectively (see Figure 5). During the analysis of experimental voltage data, it is reasonable to assume that $\rho_0 \approx \rho_i$ (see Section 3.3 for a detailed discussion). This assumption results in a simplification of the expression for the voltage drop:

$$\Delta V = \frac{I}{S'} \rho_i L_{\text{eff}} \tag{10}$$

with $L_{\text{eff}} = L_{\text{eff}}^{\alpha} + L_{\text{eff}}^{\beta}$. All of the quantities that are necessary to calculate these effective lengths are reported in Table 1. c_1, c_2, $(c_2 + c_{mid})$, c_3, c_4 and w' have been measured from the top view micrographs of each fabrication step. Since no cut has been performed in the wide region, S and w are equal to the cross-section area and to the width of the sample in the as-grown condition, respectively. It should be noticed that, while c_1, c_2 and c_4 do not change for all of the three different machining steps, as expected, this is not true for c_3 (and consequently for $c_2 + c_{mid}$), since in the third FIB process its length is highly decreased. This has been induced by the fact that, because of the relatively wide cone of extraction of the ion beam, for this machining step the width of the sample top surface has been reduced down to $0.77\ \mu m$ only, and therefore the continuity of the electrically active silver deposition has not been fully preserved in such a narrow crystal

region. For this reason, a shorter contact length has to be taken into account in order to correctly characterize the contact geometry of this fabrication step.

The obtained values for the effective lengths are reported in Table 2. We notice that L_{eff}^{β} and L_{eff}^{α} represent the effective lengths of the narrow region and of the sum of the two wide regions of the sample, respectively. Moreover, as the cross-section area is being reduced, the value of L_{eff}^{α} becomes smaller, reflecting the decreasing contribution to the transport properties of the wide contacted region of the crystal with respect to the narrow one, which features an increasing resistance.

3.3. Resistivity curves

Figure 6 shows the resistivity curves for each machining step of the sample. In the case of the sample in the as-grown condition, the resistivity is obtained with the well-known formula:

$$\rho_0 = \frac{\Delta V}{I} \frac{S}{L}. \tag{11}$$

The data analysis for the sample after the FIB processes is more intriguing. The curves reported in Figure 6 have been calculated by using the simplified expression:

$$\rho_i = \frac{\Delta V}{I} \frac{S'}{L_{\text{eff}}} \tag{12}$$

which directly comes from equation (10). Even if this expression is based upon the approximation $\rho_0 \approx \rho_i$, which makes it not fully self-consistent, it is possible to prove that such curves can be considered a very good and accurate estimate for the resistivities ρ_i. Inset B of Figure 6 focuses on the high temperature range of experimental data and compares these approximated results with the ones obtained by using the exact formula deriving from equation (7): $\rho_i = \Delta V \ S'/(I L_{\text{eff}}^{\beta}) - \rho_0 L_{\text{eff}}^{\alpha}/L_{\text{eff}}^{\beta}$, where it is assumed that ρ_0 is equal to the resistivity of the crystal in the as-grown condition, which is reasonable, as the FIB machining does not affect the wide regions. As a matter of fact, the approximated values (closed symbols) differ from the exact ones (open symbols) by about 0.4 %, which is well inside the experimental uncertainties. However, it is worth stressing the fact that the exact formula could not be applied to the whole experimental range. Indeed, by looking at inset A of Figure 6 it is clear that the sample in the as-grown condition undergoes the superconducting transition at a different temperature with respect to the steps that follow the FIB fabrications; then, in this 2 K wide temperature range it is not possible to use the curve available for the as-grown condition in order to calculate the resistivity curves for the subsequent steps.

Concerning the critical temperatures, their values have been estimated as the inflection point of the critical transition and are reported in Table 3; error bars correspond to the spacing in temperature between couples of subsequent data points in the electrical characterizations. It is apparent that these values well agree with the ones (80 K$\lesssim T_c \lesssim$ 86 K) previously measured on 10 % Ca-substituted YBCO crystals in the optimally doped regime [21, 22]. However, while the values taken after each of the three

FIB processes are all included within a 0.2 K wide range, this is not the case for the value taken for the sample in the as-grown condition, which is clearly shifted by about 1 K. This critical temperature drop suggests that an intrinsic difference exists between the sample in its natural as-grown condition and after it has undergone the FIB treatments and that this effect is not simply linear in nature. This situation somewhat resembles the one occurring for the deposition of copper on Bi-2212, where the creation of the Cu/Bi-2212 interface has been proved to affect the O $2p$ holes even for a very thin (0.3 Å) deposited Cu layer [23] and to be not linear with the layer thickness. In that case, the effect was ascribed to the electron addition from the copper atoms and this could also be the cause of the T_c decrease after the first FIB process, as a consequence of gallium implantation and radiation damage. In fact, the spatial extension of FIB irradiation damage and implantation can be estimated by the penetration range of 30 keV Ga ions into YBCO, calculated with the TRIM program [24]. As a result, the longitudinal projected range for ions impinging at normal incidence is 15 nm, while the full extension of ion distribution reaches a depth of 40 nm. This value can be taken as an upper limit of the skin depth that is damaged by the ion beam and where the Ga ions are implanted during the erosion process, modifying the electrical properties like in the case of surface Cu atoms.

The crystal in the as-grown condition features a room-temperature resistivity value of $(2.18 \pm 0.13) \, \Omega \cdot \mu$m; on the other hand, a value of about $1 \, \Omega \cdot \mu$m has been reported for Ca-doped YBCO single crystals at room temperature [22]. Considering the sequence of FIB processes undergone by the sample, a general trend showing a resistivity increase with the decrease of the cross-section area can be noticed. Unfortunately, because of the large error bars ($\sim 7\%$), a possible agreement among all of the curves cannot be ruled out. However, a careful error analysis reveals that the major source of uncertainty is represented by the error on the thickness ($\sim 6\%$), whose value is shared among all the steps. Therefore, some deeper insight can be obtained by defining the *sheet resistivity* $\rho_S = \rho/t$. By applying this definition, equations (11) and (12), which provide the sample resistivity in the as-grown and after-FIB conditions, are cast into, respectively:

$$\rho_{S,0} = \frac{\Delta V}{I} \frac{w}{L} \tag{13}$$

$$\rho_{S,i} = \frac{\Delta V}{I} \frac{\frac{1}{2}(b_M + b_m)}{L_{\text{eff}}} \tag{14}$$

It can be seen that these expressions are independent from the thickness value, thus implying that sheet resistivity is not affected by the corresponding uncertainty. A plot of ρ_S as a function of temperature is shown in figure 7. A significant sheet resistivity increase with the decrease of the cross-section area can now be inferred according to this figure. This behaviour, though being intuitive, is in contrast with the one observed in a previous work on BSCCO whiskers [6]. In order to give an interpretation for this result, some hypotheses have been considered. In literature, a phenomenon which is often invoked when dealing with size-dependent electrical properties is the inelastic electron

scattering at sample surfaces, which gives a significant contribution whenever the mean free path of the charge carriers is comparable with some physical size of the sample [25, 26, 27, 28, 29, 30]. An estimation for the mean free path in superconductors is given by: $l(T) = \lambda_S^2 \, v_F / (\epsilon_0 \, c^2 \, \rho(T))$ [31]; in the case of YBCO, the magnetic penetration depth λ_S is about 100 nm [32], while the Fermi velocity v_F is $5 \cdot 10^5$ ms^{-1} [33]. As a result, at room temperature the mean free path is about 3 nm; this value is more than two orders of magnitude smaller than the smallest sample size we are dealing with, that is the whisker width after the third FIB processing. In such conditions, surface scattering cannot account for the observed behaviour. In principle, other inelastic electron scattering sources can be grain boundaries and defects of growth like twinnings and dislocations; grain boundaries have been reported to increase the sample resistivity by many authors in the case of samples whose mean grain size is comparable with the carriers mean free path [27, 28, 34, 35]. For the present experiment, although all of the four fabrication steps of the whisker have the same morphology, both the grain size and the number density of the defects could be supposed to be different in the side regions of the crystal, which are progressively cut away by means of the FIB machining, with respect to the central region; in this case, the population of such features could be thought of as changing along the fabrication steps. An in-depth morphological study would be required in order to investigate the distribution of these inelastic scattering sources inside YBCO whiskers. However, other factors are more likely influencing the charge carrier concentration and thus the resistivity of our crystal. Among them, the oxygen out-diffusion process has already proved to play a major role in the case of BSCCO whiskers at room temperature, inducing a remarkable acceleration of the material ageing (i.e. of the resistivity increase) in low oxygen partial pressure conditions [36], even in the absence of any ion beam induced effect. In the case of YBCO, some experimental data on ion beam machined microstrips have been explained by the existence of suppressed superconductity edges [9], which is compatible with the oxygen out-diffusion process, or have been explicitly interpreted in terms of oxygen escape during the different ion beam machining steps [10]. Such evidences suggest that these phenomena could be of a general character for all of the YBCO samples whose sizes are of the same order of magnitude as the oxygen diffusion length, and that they can be possibly enhanced by ion beam induced local heating. Finally, gallium ions, which are implanted into the sample during the FIB machining process, are strongly suspected to play a major role in this phenomenon because of the relationship with the T_c changes, but further investigation is required in order to clarify the role of Ga ion as a doping species.

4. Conclusions

We have reported both the geometrical and electrical (resistivity versus temperature) characterization of four fabrication steps of a YBCO whisker sample, obtained by means of a FIB device and corresponding to decreasing cross-section areas. Through a careful analysis of the crystal morphology, it has been demonstrated that ion beam fabrication

results in a trapezoidal cross-section for the processed material, with an inclination angle of the lateral sides of about 84°. In order to correctly describe the electrodynamics related to the four-probe experimental setup, a geometrical model has been proposed, allowing an accurate calculation of the resistivity curves for all the machining steps of the whisker. An increasing behaviour of the electrical sheet resistivity with decreasing the cross-section area has been measured. Among the factors possibly responsible for such behaviour, inelastic electron scattering at sample surfaces has been excluded because of the very small mean free path of carriers in the case of YBCO. On the other hand, oxygen out-diffusion and gallium poisoning due to the FIB processing are two of the candidate processes that could explain such resistivity increase; further work is required in order to clarify their role.

Acknowledgments

References

[1] Bednorz JG and Müller KA 1986 Possible high T_C superconductivity in the Ba-La-Cu-O system, *Z. Physik. B* **64** 189–93
[2] Krasnov VM 2004 Intrinsic tunneling spectroscopy: a look from the inside at HTSC, *Physica C* **408-410** 405–9
[3] Gorlova IG and Timofeev VN 1995 The crystal structure and excess conductivity of BSCCO (2212) whiskers, *Physica C* **255** 131–5
[4] Timofeev VN and Gorlova IG 1998 Growth defects in BSCCO (2212) single crystal whiskers, *Physica C* **309** 113–9
[5] Latyshev YI, Gorlova IG, Nikitina AM, Antokhina VU, Zybtsev SG, Kukhta NP, Timofeev VN 1993 Growth and study of single-phase 2212 BSCCO whiskers of submicron cross-sectional area, *Physica C* **216** 471–7
[6] Latyshev YI, Laborde O, Monceau P 1995 The normal-state magnetoresistance of BSCCO 2:2:1:2 single-crystal whiskers, *Europhys. Lett.* **29** 495–500
[7] Gazzadi GC, Angeli E, Facci P, Frabboni S 2006 Electrical characterization and Auger depth profiling of nanogap electrodes fabricated by I_2-assisted focused ion beam, *Appl. Phys. Lett.* **89** 173112
[8] Zhao GY, Zhang HL, Chen YQ, Peng HJ 2008 Fabrication of YBCO film patterns and their properties, *Supercond. Sci. Technol.* **21** 125016
[9] Oszi Zs, Benacka S, Strbik V, Chromik S, Spankova M, Kostic I, Kleja P 2003 Properties of $YBa_2Cu_3O_x$ and $Bi_2Sr_2CaCu_2O_x$ thin film microstrips patterned by argon ion beam, *Thin Solid Films* **433** 359–62
[10] Vincenc Obona J, Chromik S, Spankova M, Oszi Zs, Kostic I 2006 C_{60} films as etching masks for creation of micrometer and submicrometer $YBa_2Cu_3O_7$ structures, *Physica C* **435** 37–40
[11] Kim SJ, Hatano T, Kim GS, Kim HY, Nagao M, Inomata K, Yun KS, Takano Y, Arisawa S, Ishii A, Takahashi S, Chen J, Nakajima K, Yamashita T 2004 Characteristics of two-stacked intrinsic Josephson junctions with a submicron loop on a $Bi_2Sr_2CaCu_2O_{8+\delta}$ (Bi-2212) single crystal whisker, *Physica C* **412-414** 1401–5
[12] Kawae T, Nagao M, Takano Y, Wang HB, Hatano T, Yamashita T 2005 Detailed characterization

for YBCO intrinsic Josephson junctions by using small-sized junctions, *Physica C* **426-431** 1479–83

[13] Pallecchi I, Pellegrino L, Bellingeri E, Siri AS, Marré D, Gazzadi GC 2008 Investigation of FIB irradiation damage in La$_0$.7Sr$_0$.3MnO$_3$ thin films, *J. Mag. Magn. Mater.* **320** 1945–51

[14] Nagao M, Sato M, Maeda H, Yun KS, Takano Y, Hatano T, Kim SJ 2003 Superconducting properties of single-crystal whiskers of (Y0.86Ca0.14Ba2Cu3Ox) grown from precursors containing calcium and tellurium, *Appl. Phys. Lett.* **82** 1899–901

[15] Rahman Khan MM, Agostino A, Cagliero S, Pastero L, Bernardi E, Truccato M Early growth condition influence on superconducting (Y,Ca)BCO whiskers, unpublished

[16] Truccato M, Rinaudo G, Manfredotti C, Agostino A, Benzi P, Volpe P, Paolini C, Olivero P 2002 Growth, contacting and ageing of superconducting Bi-2212 whiskers, *Supercond. Sci. Technol.* **15** 1304–10

[17] Lipp S, Frey L, Lehrer C, Frank B, Demm E, Ryssel H 1996 Investigations on the topology of structures milled and etched by focused ion beams, *J. Vac. Sci. Technol. B* **14** 3996–3999

[18] Olivero P, Rubanov S, Reichart P, Gibson BC, Huntington ST, Rabeau J, Greentree AD, Salzman J, Moore D, Jamieson DN, Prawer S 2005 Ion-Beam-Assisted Lift-Off Technique for Three-Dimensional Micromachining of Freestanding Single-Crystal Diamond, *Adv. Mater.* **17** 2427–30

[19] Esposito M, Muzzi L, Sarti S, Fastampa R, Silva E 2000 Determination of the resistivity components ρ_{ab} and ρ_c from multiterminal measurements in Bi$_2$Sr$_2$CaCu$_2$O$_{8+x}$ crystals, *J. Appl. Phys.* **88** 2724–9

[20] Truccato M, Agostino A, Rinaudo G, Cagliero S, Panetta M 2006 Possible dominance of the Maki-Thompson process in the fluctuation conductivity of Bi-2212 superconducting whiskers, *J. Phys.: Condens. Matter* **18** 8295–312

[21] Honma T, Yamaya K, Mori N, Tanimoto M 1996 Effects of oxygen doping and pressure on superconducting transition temperature in Y0.9Ca0.1Ba2Cu3Oy, *Solid State Comm.* **98** 395–9

[22] Masui T, Ohmichi E, Tajima S, Osada T 2005 Irreversibility field and coherence length of Ca-substituted YBCO single crystals, *Physica C* **426-431** 335–9

[23] Qvarford M, Söderholm S, Tjernberg O, Chiaia G, Nylén H, Nyholm R, Lindau I, Karlsson UO, Bernhoff H 1996 X-ray absorption study of oxygen in the high-T$_C$ superconductor Bi$_2$Sr$_2$CaCu$_2$O$_8$ near the interfaces to Cu, Ag and Au, *Physica C* **265** 113–20

[24] The Stopping and Range of Ions in Solids, edited by Ziegler JF, Biersack JP, Littmark U (Pergamon, New York, 1996)

[25] Motayed A, Vaudin M, Davydov AV, Melngailis J, He M, Mohammad SN 2007 Diameter dependent transport properties of gallium nitride nanowire field effect transistors, *Appl. Phys. Lett.* **90** 043104

[26] Sundaram VS and Mizel A 2004 Surface effects on nanowire transport: a numerical investigation using the Boltzmann equation, *J. Phys.: Condens. Matter* **16** 4697–709

[27] Marom H, Mullin J, Eizenberg M 2006 Size-dependent resistivity of nanometric copper wires, *Phys. Rev. B* **74** 045411

[28] Steinhogl W, Schindler G, Steinlesberger G, Engelhardt M 2002 Size-dependent resistivity of metallic wires in the mesoscopic range, *Phys. Rev. B* **66** 075414

[29] Soffer SB 1967 Statistical Model for the Size Effect in Electrical Conduction, *J. Appl. Phys.* **38** 1710–5

[30] Sondheimer EH 1952 The mean free path of electrons in metals, *Adv. in Phys.* **1** 1–42

[31] Mihailovic D, Kusar P, Demsar J, Kabanov VV 2006 The Determination of Length Scales Associated with Dynamic Inhomogeneity in Cuprate Superconductors, *J. Supercond. Novel Mag.* **19** 43–7

[32] Pereg-Barnea T, Turner PJ, Harris R, Mullins GK, Bobowski JS, Raudsepp M, Liang R, Bonn DA, Hardy WN 2004 Absolute values of the London penetration depth in $Y\,Ba_2\,Cu_3\,O_{6+y}$ measured by zero field ESR spectroscopy on Gd doped single crystals, *Phys. Rev. B* **69** 184513

[33] Seidel P, Grajcar M, Plecenik A, Hlubina R 1996 Superconducting parameters of YBCO and

BSCCO from 'tunneling' spectroscopy, *Physica B* **218** 224–7

[34] Mayadas AF, Shatzkes M, Janak JF 1969 Electrical resistivity model for polycristalline films: the case of specular reflection at external surfaces, *Appl. Phys. Lett.* **14** 345–7

[35] Mayadas AF and Shatzkes M 1970 Electrical-resistivity model for polycristalline films: the case of arbitrary reflection at external surfaces, *Phys. Rev. B* **1** 1382–9

[36] Cagliero S, Agostino A, Bonometti E, Truccato M 2007 Electrical transport effects due to oxygen content modifications in a $Bi_2 Sr_2 Ca Cu_2 O_{8+\delta}$ superconducting whisker, *Supercond. Sci. Technol.* **20** 667–71

Table 1. List of all the quantities necessary for the determination of the cross-section area and the effective length for each fabrication step of the sample (see text).

	AS-GROWN	FIB 1	FIB 2	FIB 3
t (μm)	3.55 ± 0.20	3.55 ± 0.20	3.55 ± 0.20	3.55 ± 0.20
w (μm)	22.35 ± 0.21	-	-	-
edge correction (μm^2)	2	-	-	-
b_M (μm)	-	5.88 ± 0.05	3.28 ± 0.06	1.65 ± 0.06
$b_m = w'$ (μm)	-	4.90 ± 0.14	2.40 ± 0.09	0.77 ± 0.06
c_1 (μm)	-	46 ± 3	46 ± 3	46 ± 3
c_2 (μm)	-	18.6 ± 1.6	17.7 ± 1.7	18.1 ± 1.5
$c_2 + c_{mid}$ (μm)	-	113.0 ± 1.9	112.2 ± 2.0	138.6 ± 2.4
c_3 (μm)	-	42.7 ± 1.7	40.8 ± 1.6	13.2 ± 2.0
c_4 (μm)	-	39 ± 3	40 ± 3	39 ± 3

Table 2. List of cross-section areas and effective lengths values for the four fabrication steps of the sample.

	AS-GROWN	FIB 1	FIB 2	FIB 3
S (μm^2)	77 ± 4	-	-	-
L (μm)	166.2 ± 1.7	-	-	-
S' (μm^2)	-	19.1 ± 1.1	10.1 ± 0.6	4.3 ± 0.3
L_{eff} (μm)	-	160 ± 3	156 ± 3	154 ± 3
L_{eff}^{α} (μm)	-	9.0 ± 0.9	5.3 ± 0.5	2.32 ± 0.23
L_{eff}^{β} (μm)	-	150.8 ± 2.4	151 ± 3	152 ± 3

**Table 3.** List of critical temperature estimates for the four fabrication steps of the sample.

	AS-GROWN	FIB 1	FIB 2	FIB 3
T_c (K)	84.6 ± 0.4	83.6 ± 0.5	83.7 ± 0.5	83.5 ± 0.2
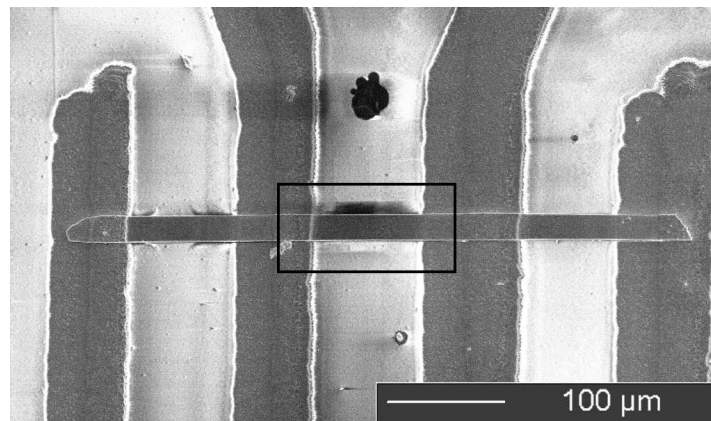
Figure 1. SEM micrograph of the crystal in the as-grown condition. The four silver plus gold strips for the electrical measurements are visible. The box highlights the region which is implied in the steps of mechanical processing.
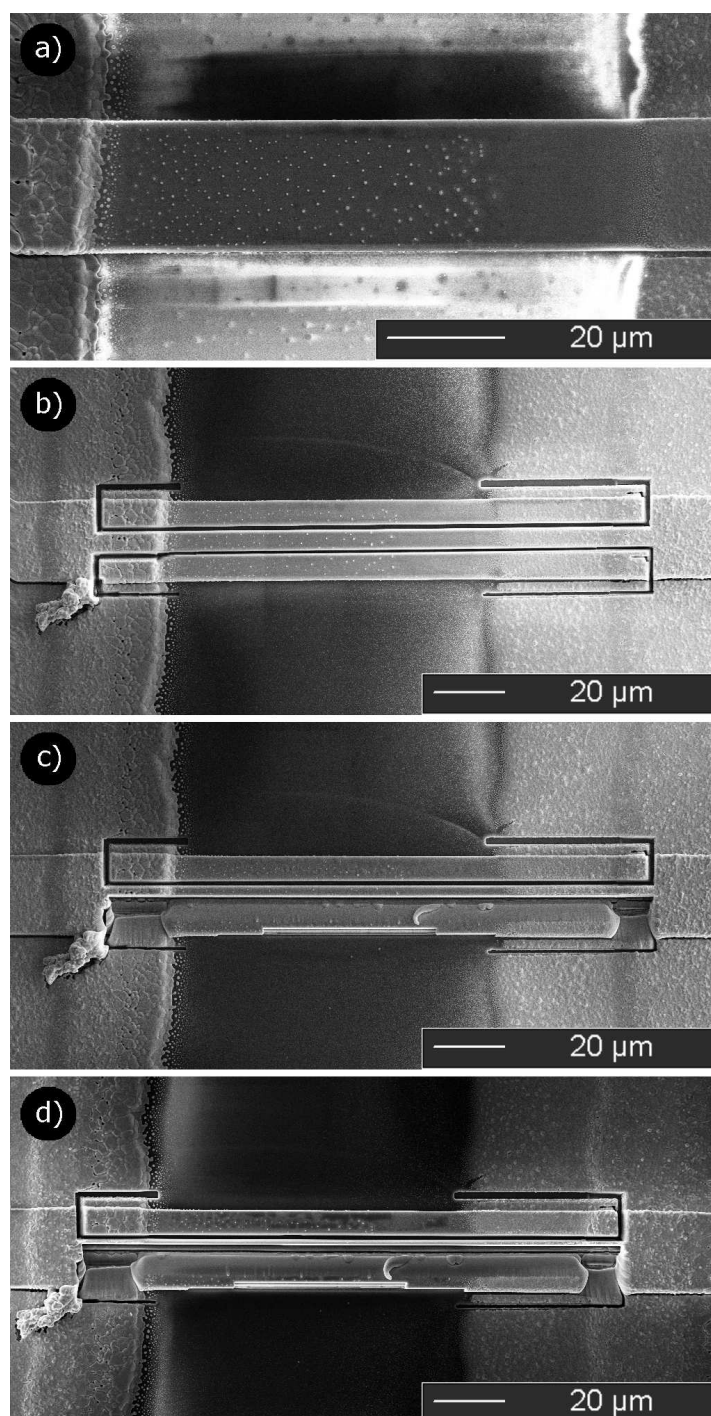
Figure 2. SEM micrographs of the region of the whisker included between the two voltage contacts. (*a*) sample in the as-grown condition; (*b*), (*c*) and (*d*) sample after the first, second and third FIB processing, respectively.
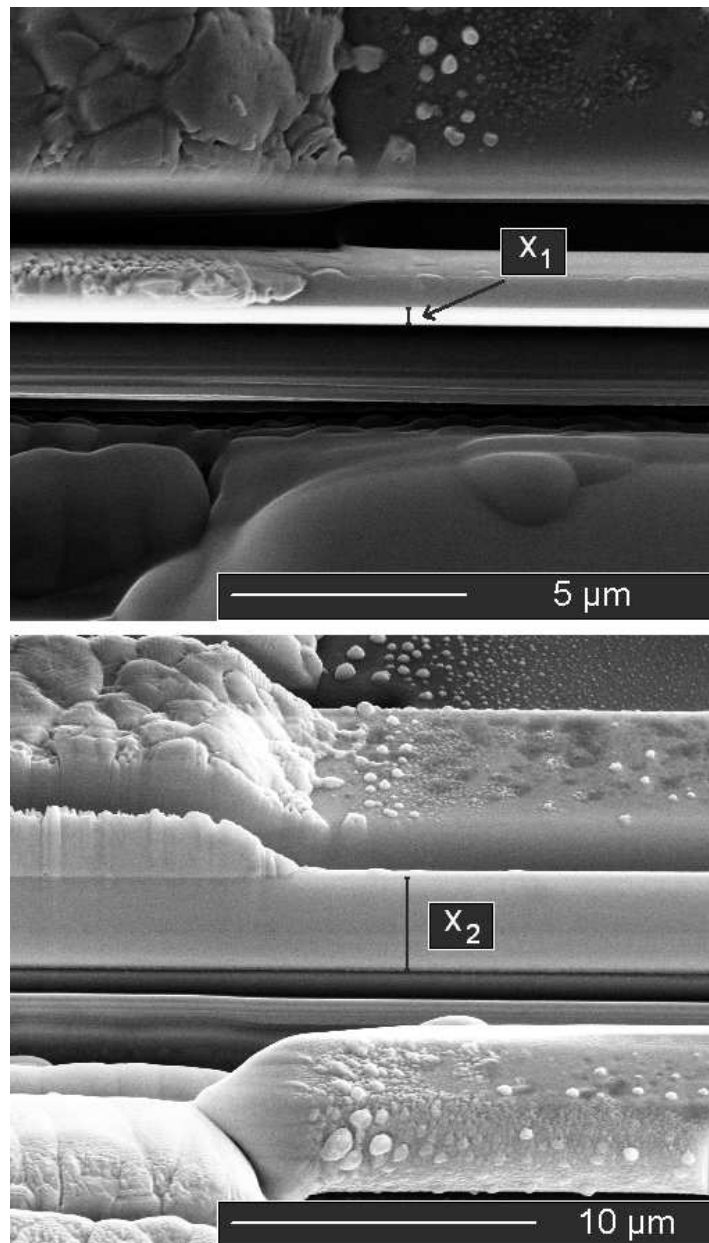
Figure 3. SEM micrographs of the whisker after the third FIB processing. The tilting angles are *a*) $\alpha_1 = 0°$ and *b*) $\alpha_2 = 52°$. Lengths corresponding to x_1 and x_2 are highlighted.
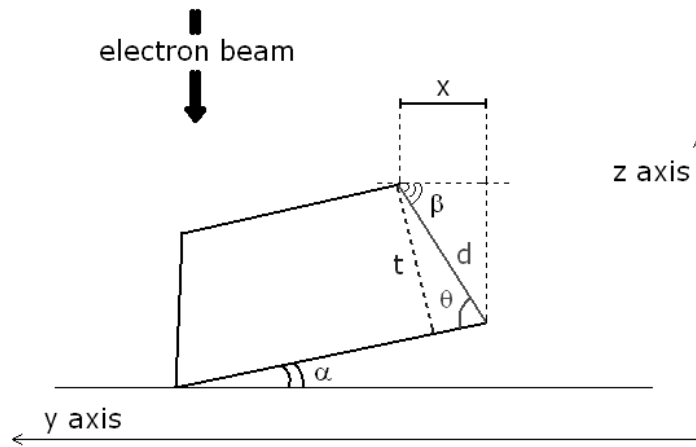
Figure 4. Schematic representation of the cross-section after the FIB processing. d and θ are the length and the inclination angle of the lateral face, respectively; t is the crystal thickness; x is the projection of d over the plane of the SEM image; x is measured from a micrograph with tilting angle α between the normal to the sample holder and the electron beam.
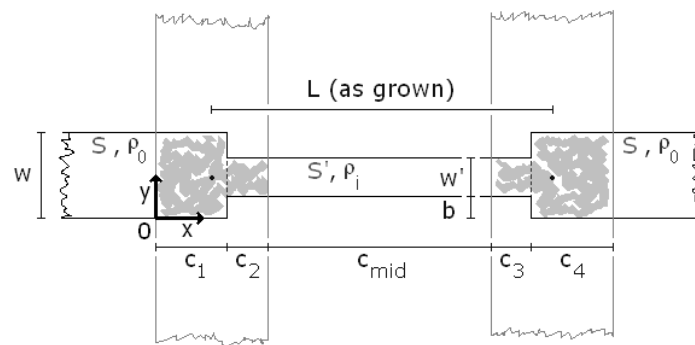
Figure 5. Schematic representation of the contacts geometry after the FIB processing. c_1, c_2, c_3, c_4, w and w' are the sizes characterizing the two voltage contacts of the crystal; c_{mid} is the distance between the two contacts. The dashed lines divide regions with different cross-sections (S and S') and assumed resistivities (ρ_0 and ρ_i); ρ_i is the resistivity of the narrow region after the ith FIB processing.
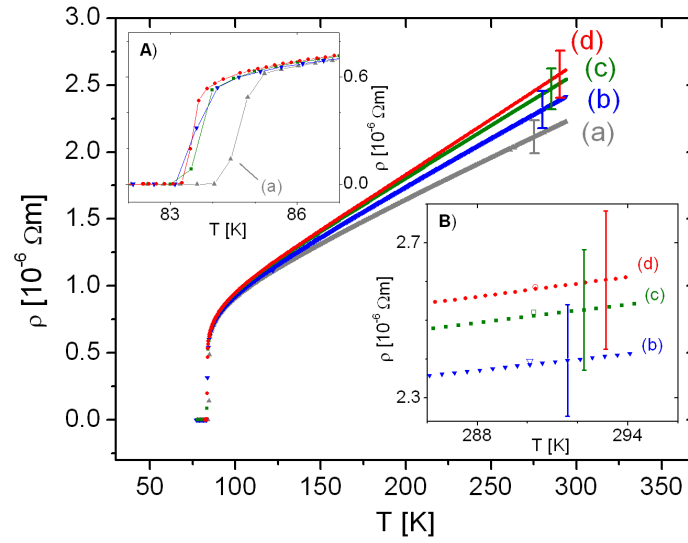
Figure 6. Comparative plot of resistivity for all of the four fabrication steps of the crystal: as-grown (a, ▲), FIB1 (b, ▼), FIB2 (c, ■), FIB3 (d, ●). Error bars are shown only for one selected temperature range to get a clear view of the data points. Inset A focuses on the temperature range of the superconductive transition. Inset B shows the data points in the room temperature range; points labeled with open symbols are obtained by means of the exact formula (see Section 3.3).
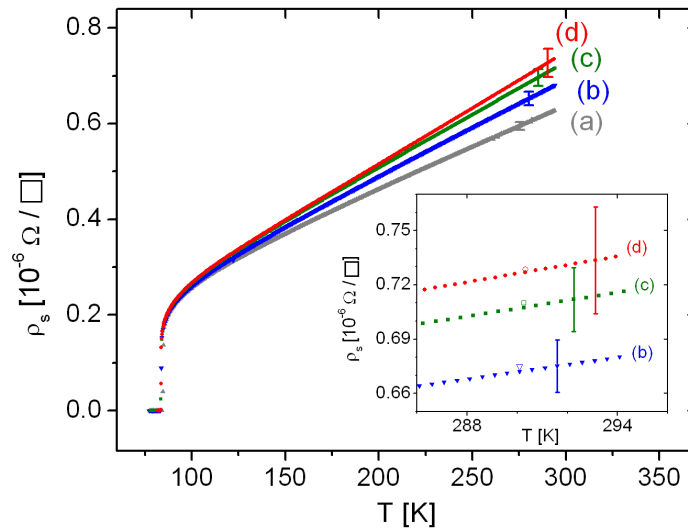
Figure 7. Comparative plot of sheet resistivity for all of the four fabrication steps of the crystal: as-grown (a, ▲), FIB1 (b, ▼), FIB2 (c, ■), FIB3 (d, ●). Error bars are shown only for one selected temperature range to get a clear view of the data points. The inset shows the data points in the room temperature range; points labeled with open symbols are obtained by means of the exact formula (see Section 3.3).